Super Resolution Microscopy and Deep Learning Identify Zika Virus Reorganization of the Endoplasmic Reticulum

Rory K. M. Long[1,2][†]**, Kathleen P. Moriarty**[3][†]**, Ben Cardoen**[3]**, Guang Gao**[1,2]**, A. Wayne Vogl**[1,2]**, François Jean**[1,4]*****, Ghassan Hamarneh**[3][‡]*****, Ivan R. Nabi**[1,2,5][‡]*****

*For correspondence:
ivan.robert.nabi@ubc.ca (IRN);
fjean@mail.ubc.ca (FJ);
hamarneh@sfu.ca (GH)

[†,‡]These authors contributed equally to this work

[1]Life Sciences Institute, University of British Columbia, Vancouver, BC, Canada; [2]Department of Cellular and Physiological Sciences, University of British Columbia, Vancouver, BC, Canada; [3]School of Computing Science, Simon Fraser University, Burnaby, BC, Canada; [4]Department of Microbiology and Immunology, University of British Columbia, Vancouver, BC, Canada; [5]5chool of Biomedical Engineering, University of British Columbia, Vancouver, BC, Canada

---

Abstract   The endoplasmic reticulum (ER) is a complex subcellular organelle composed of diverse structures such as tubules, sheets and tubular matrices. Flaviviruses such as Zika virus (ZIKV) induce reorganization of endoplasmic reticulum (ER) membranes to facilitate viral replication. Here, using 3D super resolution microscopy, ZIKV infection is shown to induce the formation of dense tubular matrices associated with viral replication in the central ER. Viral non-structural proteins NS4B and NS2B associate with replication complexes within the ZIKV-induced tubular matrix and exhibit distinct ER distributions outside this central ER region. Deep neural networks trained to identify ZIKV-infected versus mock-infected cells successfully identified ZIKV-induced central ER tubular matrices as a determinant of viral infection. Super resolution microscopy and deep learning are therefore able to identify and localize morphological features of the ER and may be of use to screen for inhibitors of infection by ER-reorganizing viruses.

Introduction

The endoplasmic reticulum (ER) is a highly dynamic network composed of 30-100 nm ribosome-studded rough ER sheets and convoluted networks of smooth ER tubules (1, 2). ER shaping proteins such as the lumenal sheet spacer protein cytoskeleton-linking membrane protein 63 (CLIMP-63), membrane curvature stabilizing reticulons (RTN) and junction stabilizing atlastin (ATL) are responsible for the generation of the morphologically distinct domains that comprise the ER (2-4). Recently, 2D STimulated Emission Depletion microscopy (STED) super-resolution microscopy combined with high-speed live cell or rapid fixation approaches showed that RTN and CLIMP-63 regulate not only the ER macrostructure of rough ER sheets vs smooth ER tubules but also the nanodomain organization of sheets and tubules imaged in the cell periphery (5, 6). Increasing both 3D spatial and temporal resolution with various super resolution imaging techniques, including 3D structured illumination (SIM), grazing incidence structured illumination (GI-SIM) and lattice light sheet point accumulation for imaging in nanoscale topography (LLS-PAINT), showed that peripheral sheets were

40 actually dense tubular matrices (7). While application of super-resolution microscopy to define
41 morphology of peripheral ER (PER) structures has proven fruitful, its use to study the central ER
42 (CER), and changes associated with cellular stressors has proven more challenging.

43 The ER is often utilized by pathogens to subvert the cytoplasmic innate immune response and
44 promote replication (8-10). Bacteria, such as *Legionella pneumophila* and *Brucella abortus*, RNA
45 viruses, and some intracellular protist pathogens, such as *Toxoplasma gondii*, all utilize the unique
46 functions of the ER to promote their own replication (11-13). Flaviviruses, and coronaviruses, re-
47 organize ER membranes into novel structures to better facilitate viral replication (12, 14, 15). A
48 well-studied ER reorganizing flavivirus is the Zika virus (ZIKV), a member of the flavivirus genera
49 within the *Flaviviridae* viral family that includes the dengue virus (DENV), and has shown causative
50 association with congenital microcephaly and other neurological diseases (16-18). ZIKV-induced
51 ER structures include replication factories, 60-100 nm spherical vesicular invaginations within the
52 rough ER lumen that contain viral double-stranded RNA (dsRNA), an intermediate in genomic repli-
53 cation, that are the site of viral RNA genomic replication (19, 20). Associated with replication facto-
54 ries are ZIKV-induced convoluted networks of ER tubules, known as convoluted membranes, that
55 are for the most part smooth although rough convoluted membranes containing replication facto-
56 ries have been reported in neural progenitor cells (19, 21).

57 The ZIKV RNA genome encodes 10 proteins, corresponding to the DENV genome, including 3
58 structural proteins (Capsid (C), Membrane (prM/M), and Envelope (E) proteins), involved in assem-
59 bly of the virus capsid and envelope, and 7 non-structural (NS) proteins (NS1, NS2A, NS2B, NS3,
60 NS4A, NS4B, and NS5) (22, 23). The NS proteins form the replication complexes and play key roles
61 in the evasion of the host innate immune response, the hijacking of host cellular pathways, and the
62 reorganization of ER membranes to promote viral replication (24). All of the flaviviral NS proteins
63 are believed to play a role in the formation of the genomic replication machinery and replication
64 factories. ZIKV NS3 and NS4B have been shown to overlap with convoluted membranes and repli-
65 cation factories by light microscopy (19, 25). NS2B is an integral membrane protein which localizes
66 NS3 to replication factories and functions as a cofactor for the protease activity of NS3; NS2B and
67 NS3 localize to both convoluted membranes and replication factories by electron microscopy (EM)
68 (19, 26-28). NS4B is a transmembrane protein with five integral transmembrane domains, previ-
69 ously shown to be involved in the formation of convoluted membranes in DENV-infected Huh7
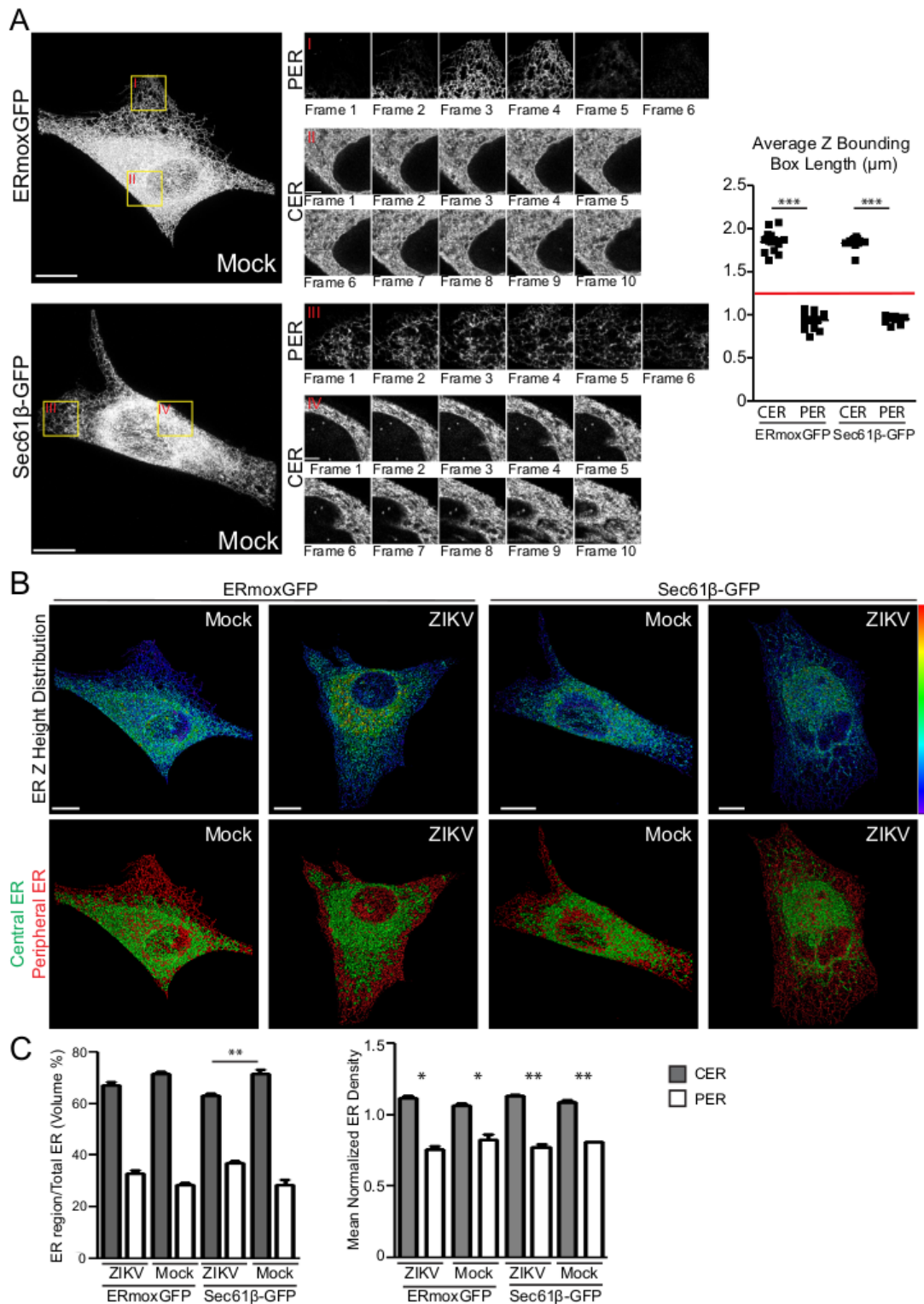70 cells (26).

71 Virus-induced ER structures have been well-characterized by EM, however the cellular distribu-
72 tion of these structures and associated viral proteins remains poorly understood. Here, we use 3D
73 STED super-resolution microscopy to show that ZIKV infection induces the reorganization of the
74 CER to form dense tubular matrices associated with ZIKV replication sites. We further apply deep
75 learning approaches to identify ZIKV-infected cells based on changes in ER morphology. Quantita-
76 tive detection of virus-induced changes to the ER represents proof-of-principle for the application
77 of deep learning-based image analysis of ER reorganization for large scale drug screening and iden-
78 tification of compounds inhibitory to viral infection.

Results

ZIKV infection induces the formation of a dense tubular matrix in the CER

81 In order to study ER morphology following ZIKV infection, we first generated stable U87 glioblas-
82 toma cells transfected with either ER monomeric oxidizing environment-optimized green fluores-
83 cent protein (ERmoxGFP), a lumenal ER reporter containing the bovine prolactin signal sequence
84 and KDEL ER retention sequence linked to inert, monomeric, cysteine-less moxGFP (29), or the
85 membrane-associated ER reporter Sec61β-GFP. U87 cells stably expressing the ER reporters were
86 then infected with ZIKV strain PRVABC59 (Puerto Rico 2015) at a multiplicity of infection (MOI) of 1
87 for 48 hours. Cells were fixed with 3% paraformaldehyde/0.2% glutaraldehyde to preserve ER archi-
88 tecture (6, 7, 30, 31) and labeled for dsRNA, a marker for ZIKV replication factories (19). Maximum

Figure 1. 3D STED microscopy reveals ZIKV-induced ER reorganization in human U87 glioblastoma cells. A) ERmoxGFP or Sec61β-GFP stably transfected U87 cells were mock-infected or infected for 48 hours with the PRVABC59 2015 ZIKV strain (MOI= 1). ER reporter GFP and immunostained dsRNA-labeled ZIKV replication factories were imaged by 3D STED microscopy. B) Fluorescence intensity of ERmoxGFP of infected cells using a spectrum heat map and a segmentation mask of the ER that colocalizes with dsRNA (grey), both generated on Imaris x64 9.2.1 (Imaris), are depicted. Yellow squares in the panels indicate the magnified ROIs shown in the adjacent panels. Quantification of the mean normalized ER density ((Intensity sum of mask/total cell intensity sum)/ (volume sum of mask/ total cell volume sum)) was performed for both dsRNA-positive and dsRNA-negative ERmoxGFP and Sec61β-GFP in ZIKV-infected cells by Imaris segmentation. Scale bar= 10 microns. 5 cells per biological replicate (N=3). Statistics were done using unpaired Student's T tests: **= P<0.01, Error bars represent SEM.
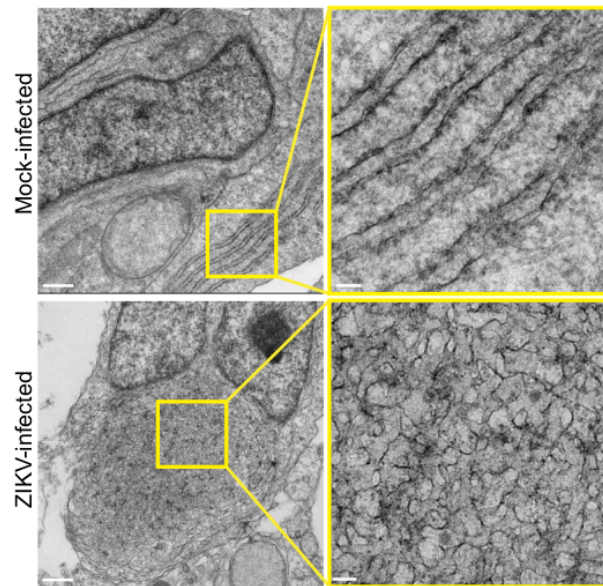
Figure 2. Defining the CER and PER of ZIKV- and mock-infected cells. A) Mock-infected ERmoxGFP and Sec61β-GFP stably transfected U87 cells were imaged by 3D STED microscopy. Magnified ROIs (yellow ROIs identified by red Roman numerals) show that the PER extends over 3-5 sections (210 nm step size) and CER >10 sections. Graph shows average PER and CER Z-height for each ERmoxGFP or Sec61β-GFP labeled cell. A Z-height cutoff of 1.26 microns (red line) was used to identify PER and CER objects. B) Segmented ER labeling from 48-hour ZIKV- or mock-infected ERmoxGFP or Sec61β-GFP stably transfected U87 cells (MOI= 1) was visualized using a Z-height spectrum heat map and CER (green; > 1.26 μm) and PER (red; < 1.26 μm) masks are shown. C) Volume percentage (left) and mean normalized density (right) of CER and PER masks between mock- and ZIKV-infected cells. 5 cells per biological replicate were analyzed for a total of N=3. ANOVA with post-hoc Tukey HSD: *= P<0.05, **= P<0.01, and ***= P<0.001. Error bars represent SEM. Scale bar= 10 microns.
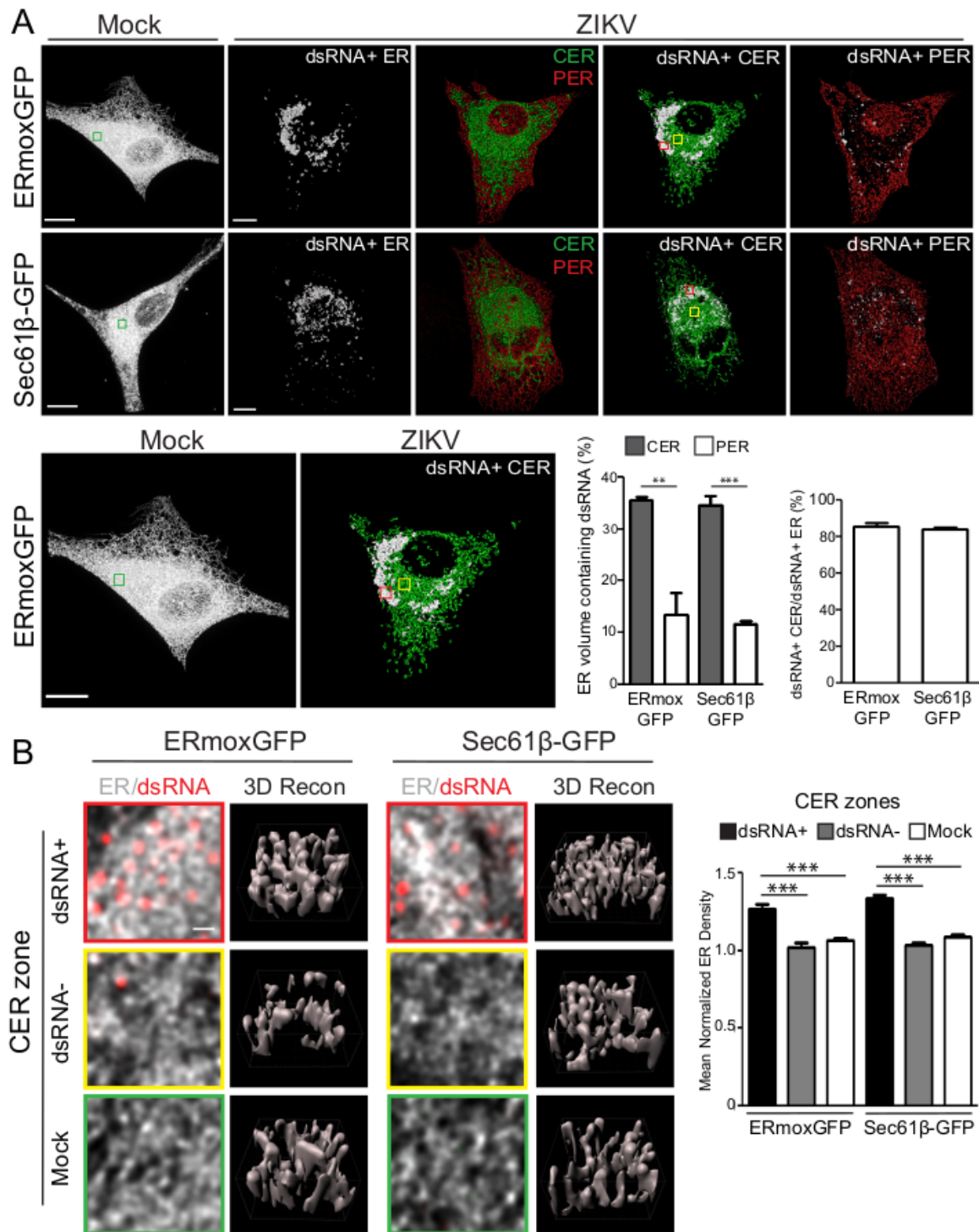
Figure 3. The ZIKV-induced dsRNA-positive CER region is a dense tubular matrix. A) Shown are representative mock-infected cells and CER (green) and PER (red) masks overlaid with the dsRNA-positive ER mask (white) for ZIKV-infected ERmoxGFP and Sec61β-GFP transfected U87 cells. Enlarged images of ERmoxGFP transfected cells show 3x3 μm ROIs of the mock-infected CER (green box) and of the ZIKV-infected dsRNA-positive (red box) and dsRNA-negative (yellow box) CER shown in B. Graphs show the volume percent of the CER or PER region that contains dsRNA-positive ER (left) and the volume percent of the dsRNA-positive ER that resides within the CER mask. B) 2D images of ER (white) and dsRNA (red) labeling in 3x3 μm ROIs of the ZIKV-infected dsRNA-positive (red) and dsRNA-negative (yellow) CER and mock-infected (green) CER are shown above Imaris 3D surface rendering of 1x1 μm regions of the above ROIs. Graph shows mean normalized ER density for each of the three CER zones by Imaris segmentation and masking. 5 cells per biological replicate were analyzed for a total of N=3. ANOVA with post-hoc Tukey HSD: *= P<0.05, **= P<0.01, and ***= P<0.001. Error bars represent SEM. Scale bar: 10 microns (500 nm for zoomed ROIs).

projections of 3D STED image stacks show high intensity ERmoxGFP and Sec61β-GFP labeling in a CER region and low intensity labeling in PER tubules in mock-infected cells (Figure 1A), as reported previously by diffraction limited confocal microscopy (3). Upon ZIKV infection, the CER reorganizes to form an intensely labeled crescent-shaped region surrounding a lower intensity perinuclear region (Figure 1A). Interestingly, the crescent-shaped ZIKV-induced perinuclear ER overlapped extensively with dsRNA (Figure 1A). Imaris Bitplane software fragments the ER into distinct segments that can then be analyzed for different features, including reporter density, segment Z-height and segment overlap with other labels, such as dsRNA. Density-based segmentation of the ERmoxGFP- and Sec61β-GFP-labelled ER of ZIKV-infected cells showed that the higher density crescent-shaped CER region exhibited significant overlap with dsRNA-positive ER structures relative to the rest of the ER (Figure 1B). This suggests that ZIKV dsRNA associates with an ER region of high density for both lumenal and membrane ER reporters.

We then investigated the relationship between the dense ZIKV-induced crescent-like region and the CER and PER. Segmenting the ER based on Z-height of ER segments showed that PER tubules were present in 3-5 consecutive frames of 210 nm each while CER regions were abundantly present across 7-10 consecutive frames (Figure 2A). For both ERmoxGFP and Sec61β-GFP labeled cells, average max Z-height of PER tubular regions was 0.95 μm and for CER regions 1.8 μm (Figure 2A). No PER segments reached a height greater than 1.26 μm. ER segments with a height above 1.26 μm were therefore classified as CER and ER segments with a height below 1.26 μm as PER, effectively segmenting the ER into CER and PER regions (Figure 2B). Based on this ER segment height-based classification of CER and PER, the CER was found to present a two-fold increase in volume and increased density relative to the PER (Figure 2C). ER density in the height-based CER was elevated relative to PER and ZIKV infection showed minimal impact on the relative volume or density of CER and PER regions (Figure 2D).

Figure 4. Ultrastructural analysis of ZIKV-infected cerebral brain organoids. Transmission EM images of 50 nm thin sections of 48-hour mock- and ZIKV-infected cerebral brain organoids (MOI=1). Yellow boxes show ROIs shown of adjacent higher magnification images that highlight rough ER sheets in mock-infected and tubular matrices (convoluted membranes) in ZIKV-infected cells. Scale bars: 500 nm and 100 nm for zoomed image ROIs.

Overlaying the CER and PER masks with the dsRNA-positive ER mask showed that the dsRNA-positive ER (>80% volume/volume) is predominantly included within the CER mask (Figure 3A). Indeed, only 10% of PER volume contains dsRNA while 35% of CER volume contains dsRNA for both ER reporters (Figure 3A). Morphological comparison of the dsRNA-positive and -negative CER of ZIKV-infected cells with the CER of mock-infected cells showed that the CER was composed of a convoluted network of tubules for both the ERmoxGFP- and Sec61β-labeled ER (Figure 3B). 3D reconstructions confirmed that these regions were predominantly tubular with a few small sheet-like structures, similar to the tubular matrix morphology of peripheral sheets (7). 3D voxel-based visualization and quantification showed that the density of ER tubular structures in the dsRNA-positive ER is higher, for both the ERmoxGFP or Sec61β-GFP ER reporters, than in the dsRNA-negative CER

140 regions of ZIKV-infected cells or the CER of mock-infected cells (Figure 3B). The lower ER reporter
141 density reflects reduced spacing between tubules in the dsRNA-positive ER, suggesting that ZIKV
142 infection induces tubular matrix reorganization in a subdomain of the CER in U87 cells. Consis-
143 tently, EM analysis of the microcephaly relevant cerebral brain organoid model (32) showed that
144 ZIKV-induced ER reorganization from perinuclear stacked rough ER sheets to a perinuclear, circular
145 region of convoluted smooth ER tubules (Figure 4). These results are consistent with ZIKV induction
146 of a perinuclear tubular matrix.

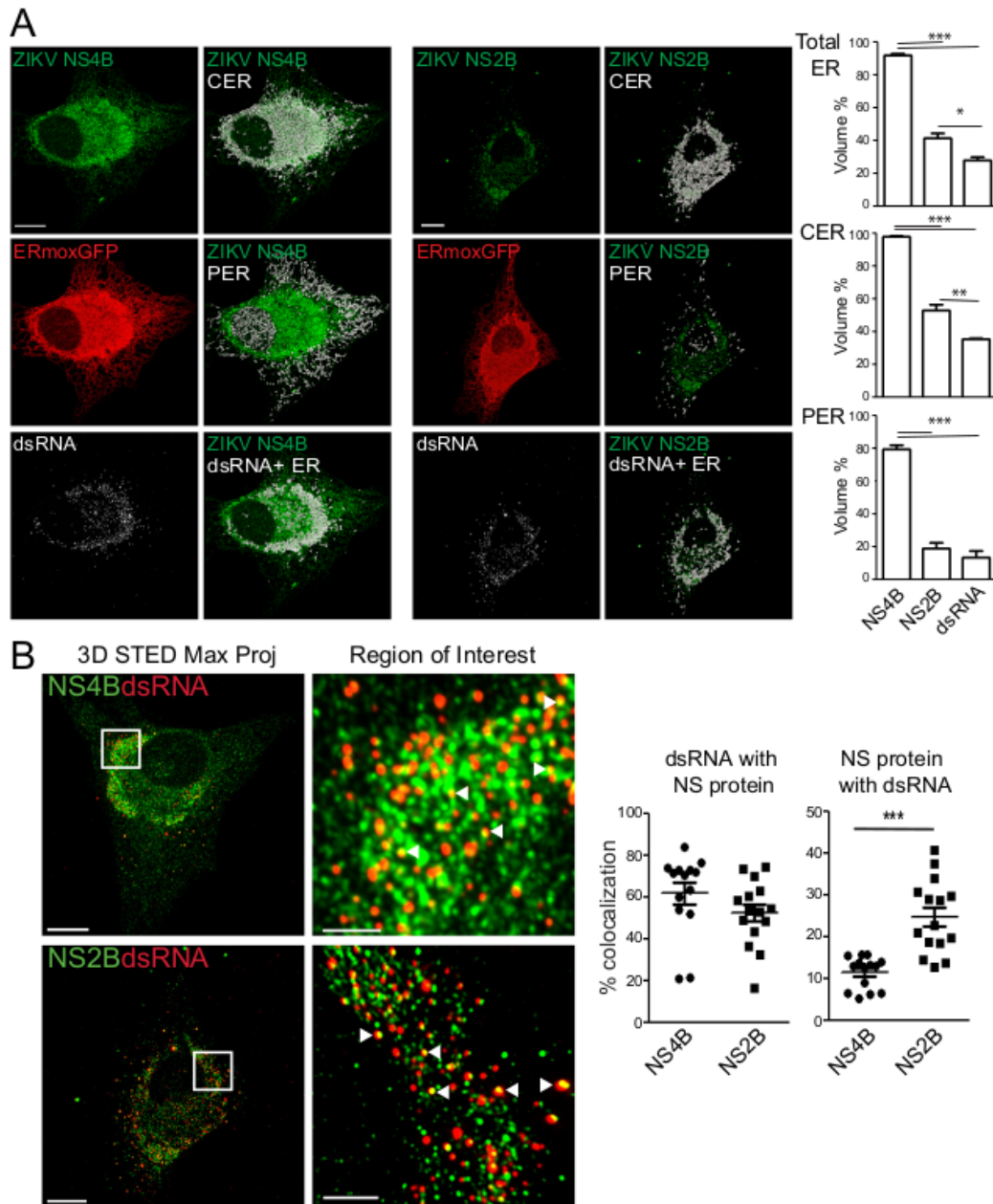### 147 ER localization of ZIKV NS2B and NS4B structural proteins

148 We then labeled cells for ZIKV NS proteins NS2B and NS4B to assess their relationship to the ZIKV-
149 induced tubular matrix. 3D STED analysis showed a predominant distribution of both NS2B and
150 NS4B to the CER and more particularly to the dense ZIKV-induced crescent-shaped tubular matrix
151 in ERmoxGFP transfected U87 cells (Figure 5A). While NS2B is predominantly associated with the
152 dsRNA-positive CER, NS4B labeling extended throughout the CER as well as to the PER (Figure 5A).
153 To quantify this, we identified NS2B-positive and NS4B-positive ER segments and determined their
154 overlap with total ER, CER and PER (Figure 5A). While NS4B was present at high levels on both PER
155 and CER segments, NS2B was enriched in the CER relative to the PER and presented a similar ER
156 distribution to dsRNA (Figure 5A).

157 The majority (>55%) of dsRNA-labeled puncta were associated with NS2B or NS4B, consistent
158 with the presence of both these NS proteins in the ZIKV-induced tubular matrix. In contrast, a
159 minority of NS2B (~25%) and NS4B (~10%) spots overlapped with dsRNA spots (Figure 5B). In the
160 dsRNA-positive CER, the highly punctate NS2B labeling differed from a more reticular NS4B label-
161 ing. These two ZIKV NS proteins therefore exhibit distinct distributions within the ZIKV-induced
162 tubular matrix when not associated with dsRNA replication complexes (Figure 5B). Together with
163 the differential distribution of NS2B and NS4B within the ER as a whole (Figure 5A), these results
164 highlight that these two ZIKV NS proteins do not associate exclusively with replication factories and
165 suggest that following synthesis of the ZIKV polyprotein, NS2B and NS4B undergo distinct biosyn-
166 thetic pathways before reuniting in ER-associated replication complexes.

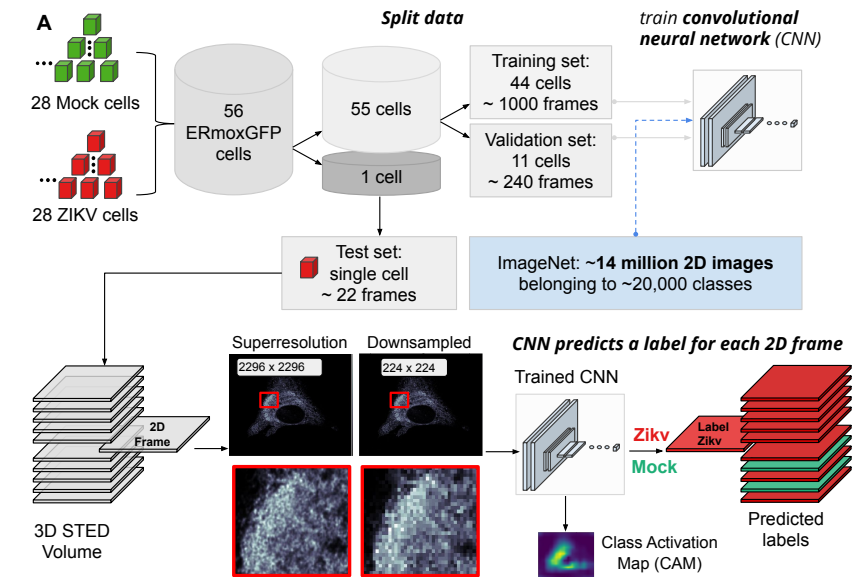### 167 Deep learning identifies ZIKV-induced ER reorganization

168 Deep learning has been successfully applied to the task of image recognition, distinguishing the
169 category or class to which a given image belongs. Deep learning architectures have outperformed
170 shallow architectures when benchmarked on ImageNet a dataset widely used by the computer
171 vision community that contains roughly 14 million images belonging to 20,000 classes (e.g., cats,
172 dogs, plant species, various modes of transportation) (33-35). Deep convolutional neural networks
173 (CNNs) are capable of learning local and global spatial patterns from raw training data (i.e. pairs of
174 images and corresponding classes) enabling inference of the correct class of unseen images, and
175 have achieved state of the art performance when benchmarked on ImageNet (36). Importantly,
176 compared to non-deep learning detection methods such as machine learning, deep learning ap-
177 proaches: 1) avoid the need to design and select features for highly complex ER structures that
178 are required by non-deep learning methods; and 2) provide the ability to move beyond simple
179 classification to inspect discriminative regions (i.e. subregions of the ER within each cell).

180 We therefore applied deep neural networks to identify and distinguish the morphological fea-
181 tures of the ER of ZIKV-infected cells. A pipeline outlining our approach is shown in Figure 6A. We
182 train a CNN using 2D frames (each representing a single Z-frame) from 3D STED volumes of ER-
183 moxGFP and Sec61B-GFP labeled ZIKV- and mock-infected cells. Our CNN builds off of VGG16, a
184 deep neural network architecture proposed by Simonyan et al. (35) which achieved state of the
185 art results on the 2014 ImageNet Large Scale Visual Recognition Challenge (ILSVRC) (37, 38). To
186 improve computation time, we initially performed the analysis on downsampled STED images. As
187 the 3D STED data sets were relatively small to train the CNN from scratch, we leveraged a network
188 already pretrained on natural images. This transfer learning technique speeds up the convergence
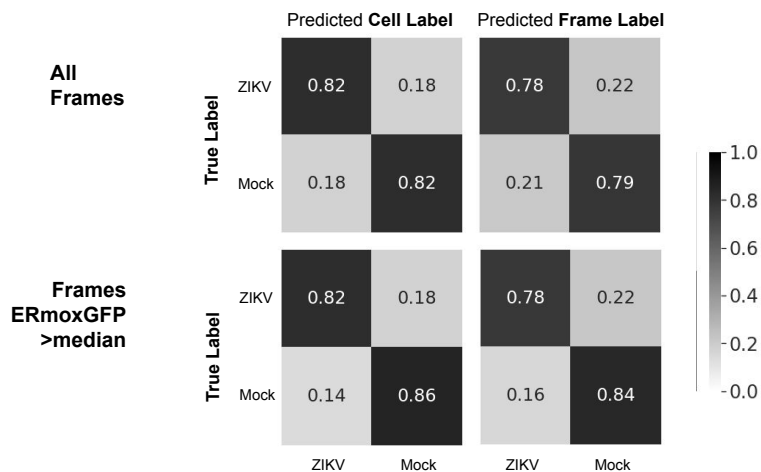
Figure 5. ER distribution of ZIKV NS2B and NS4B proteins. A) Mock- or ZIKV-infected ERmoxGFP (red) stably transfected U87 cells were immunostained for ZIKV NS2B or NS4B (green) and dsRNA (white). Merged images show NS2B or NS4B (green) overlaid with the CER, PER or dsRNA-positive ER (white). Graphs show quantification of volume percent of NS4B, NS2B and dsRNA ER regions relative to total ER, CER or PER. B) Mock- or ZIKV-infected ERmoxGFP stably transfected U87 cells were immunostained for ZIKV NS4B or NS2B (green) and dsRNA (red). White squares show ROIs of adjacent zoomed images in which white arrowheads show colocalization between NS protein and dsRNA puncta. Graphs show percent of dsRNA puncta overlapping NS4B or NS2B puncta (left) and percent of NS4B or NS2B puncta overlapping dsRNA puncta. 5 cells per biological replicate (N=3) with each dot representing a cell. ANOVA with post-hoc Tukey HSD: *=P<0.05, **=P<0.01, and ***=P<0.001. Error bars represent SEM. All images are maximum projections from 3D STED stacks. Scale bar= 10 microns. ROI scale bar = 2 microns.

189   rate of networks when dealing with small target datasets. Certain filters (combinations of weights)
190   learned on the first dataset (i.e. ImageNet) may still be useful for classifying a second dataset
191   (i.e. STED); as a result, less weight updates are needed before achieving good performance. Us-
192   ing a pretrained VGG16 as our base model we obtained a 20% boost in test accuracy, compared
193   against a random weight initialization. Using ERmoxGFP labelled ER alone, the CNN was able to
194   distinguish between ZIKV- and mock-infected cells with an 82% accuracy (Figure 6B, top left). Ac-

Figure 6. Deep learning classification pipeline: Pretrained convolutional neural network accurately predicts labels of 2D frames from 3D STED volumes. A) Leave-one-out cross validation is successively applied to each cell. This prevents information from 2D frames leaking between training, validation and test sets. During training, network uses 2D frames from 55 cells (specifically, 44 for training and 11 for validation). The trained CNN then predicts a class label (i.e. ZIKV-infected or mock-infected) to each 2D frame of the remaining test cell. Class Activation Maps are also generated for each 2D frame belonging to the test set. B) CNN performance reported on a cell basis and across 2D frames. Normalized confusion matrices report the total number of predicted labels (ZIKV-infected or mock-infected) over the total number of ground truth labels. For example, 79% of all mock-infected 2D frames were predicted correctly by the CNN (top right). Predicted cell labels correspond to the majority label of predicted frame labels for each cell (top left). When excluding frames beyond the cell with reduced ERmoxGFP signal, performance metrics increase both in terms of cell label predictions (bottom left) and individual frame label predictions (bottom right).

195 curacy using Sec61β-GFP labelled ER was only 66%, whereas combining cells labeled with both
196 ER markers, increasing the number of training samples seen by the network, still resulted in only
197 71% accuracy. Based on the improved classification performance, further analysis was performed
198 using ERmoxGFP labelled cells.
199   With a limited sample size of 56 ERmoxGFP labelled cells, we applied leave-one-out cross vali-
200 dation; 56 cells were split into a set of 55 cells used to train the CNN, and a test set consisting of
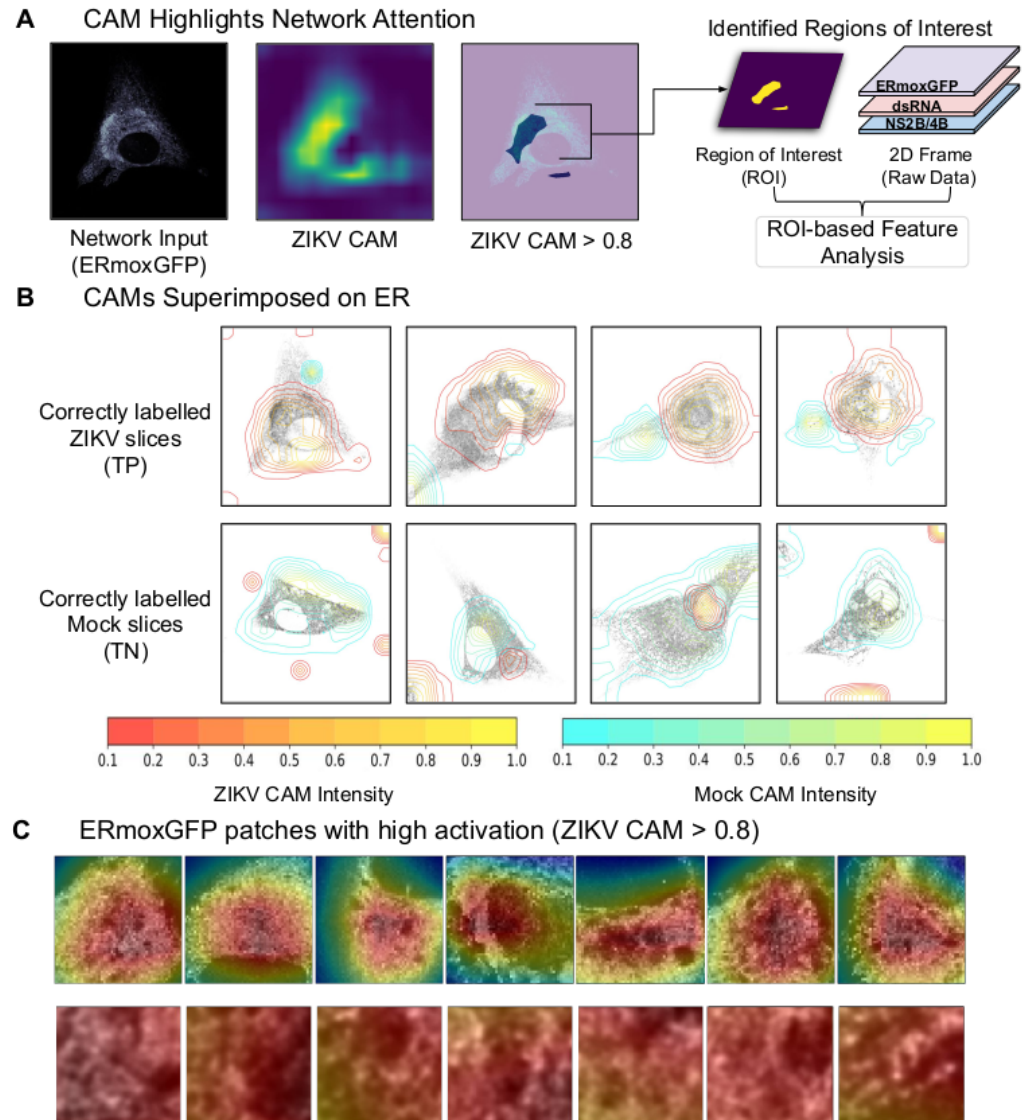
Figure 7. Class Activation Mapping for Region of Interest Based Feature Analysis. A) For each test 2D frame passed as input to the CNN, we generated Class Activation Maps (CAM) which are then thresholded to create ROIs. These regions identified by deep learning are then used for further analysis of ERmoxGFP, dsRNA and NS2B/4B. B) Contour maps of CAMs superimposed on ERmoxGFP labelled ER show regions identified by CAMs. The contour color represents varying CAM intensity from 0.1 (low network attention) to 1.0 (high network attention). For correctly labelled ZIKV-infected and mock-infected 2D frames, we show that the respective CAM focuses on the cell. C) The top row shows representative downsampled images from true positive (TP) instances highlighting the 0.8 ZIKV CAM in red. The bottom row shows 112x112 pixel patches from high resolution STED images within the 0.8 ZIKV CAM region.

201 the remaining cell. This process is outlined in Figure 6A, and is repeatedly applied using each cell
202 as the test set. The 55 cells used to train the CNN are further split into a training and validation
203 set, composed of 44 and 11 cells, respectively. During training, all 2D frames from cells belonging
204 to the training set are passed individually to the CNN while 2D frames of the validation set cells
205 are used to evaluate the performance and update the network's parameters (weights) accordingly.
206 This grouping of cells into training, validation and test sets ensures that information is not leaked,
207 i.e., the CNN is only presented with unseen 2D frames during testing. ZIKV- and mock-infected
208 class activation maps (CAMs) (39) are generated for each 2D frame to help define regions used by
209 the CNN when inferring a class label (ZIKV or Mock). We achieved 82% accuracy and 82% specificity
210 to identify ZIKV- and mock-infected cells based on a majority of frame predictions per cell. STED Z
211 stacks extend beyond the cell and include Z sections that contain minimal ERmoxGFP signal and
212 show poor accuracy to predict class label (Supp Fig 1). When considering those frames containing
213 ERmoxGFP signal intensity greater than the median, we achieved 84% accuracy and 86% sensitiv-
214 ity. On a per frame basis, accuracy for all frames was 78% and sensitivity 79% that increased to
215 81% and 84%, respectively, when considering frames expressing ERmoxGFP greater than median
216 intensity (Figure 6B, Supp. Fig. 1). Considering the confusion matrix for all frames, cell label (Figure
217 6B, top left), the 82% of ZIKV-infected 2D frames correctly predicted to be infected represent true
218 positives (TP) while the 18% of ZIKV-infected 2D frames not predicted to be infected represent false
219 negatives (FN). The 82% of mock-infected 2D frames correctly predicted to be uninfected represent
220 true negatives (TN) and the 18% of mock-infected 2D frames predicted to be ZIKV-infected repre-
221 sent false positives (FP). The CNN has therefore accurately predicted which cells are ZIKV-infected
222 based on the reorganization of ERmoxGFP-labeled ER. Improved accuracy for frames expressing
223 higher ERmoxGFP highlights that the network is using the ERmoxGFP label to identify ZIKV-infected
224 frames and cells.

225   To determine the basis for CNN decision making we analyzed the respective CAMs for both
226 classes, ZIKV- and mock-infected cells. This method, first proposed by (39) produces a heatmap (or
227 CAM), corresponding to a given image input, which can help localize the discriminating regions of
228 the image that the CNN uses to infer a class label (Figure 7A). For instance, identification of ZIKV-
229 infected slices (true positive; TP; orange) is primarily based on regions highlighted by the ZIKV CAM
230 while identification of mock-infected cells (true negative; TN; green) is based on the mock CAM
231 (Figure 7B). The range of values of the generated CAMs is between 0 and 1. Class activation maps
232 have been used for weakly supervised segmentation, i.e. to delineate regions of interest (ROIs) (40,
233 41) We consider regions of interest (ROIs) to be areas of the CAM with values greater than 80%
234 of the maximum. For example, if a CAM has maximum value of 1, the CAM thresholded at 80%
235 considers only CAM regions with values greater than 0.8, corresponding to regions of high network
236 attention. Representative examples of ZIKV (red) and mock (blue) CAMs are shown in Figure 7B; as
237 they transition to yellow, concentric rings correspond to smaller CAMs and increasing thresholds
238 from 10-95%. In general, the mock CAM was centered over the cell for correctly labelled uninfected
239 cells (TN) cells as was the ZIKV CAM for correctly labeled ZIKV-infected cells (TP) cells (Figure 7B).
240 Representative downsampled ERmoxGFP-labeled images from true positive (TP) instances show
241 the 80% ZIKV CAM in red covering the central ER region. Higher resolution TP patches (112x112
242 pixels) from these regions of high network attention (ZIKV CAM with a threshold of 80%) show ER
243 structures used to correctly label ZIKV-infected cells (Figure 7C).

Deep learning identifies ZIKV-infected cells based on the high density CER

245 As seen in Figure 8A, ROIs identified by the ZIKV CAM show consistently higher ER density at all
246 thresholds when comparing correctly identified infected frames (TP, orange) to the mock-infected
247 frames (TN, green). Similarly, for 2D frames correctly identified as mock-infected (TN), the regions
248 found by the mock CAM show increased ER density at all thresholds compared to the TP frames.
249 This suggests that the CAMs used to identify both ZIKV- and mock-infected cells correspond to high
250 ER density regions localized over the cell (see Figure 7B) and that VGG16 is using differences in the

251 ER label (ERmoxGFP) to identify slices as either ZIKV- or mock-infected. Consistently, the density
252 profile of the ZIKV CAM for cells falsely identified to be infected (false positive; FP; blue) matched
253 that of TP (orange) ZIKV-infected cells while that of the mock CAM for cells falsely identified to be
254 uninfected (false negative; FN; purple) matched the mock TN (green) profile. ER density for the ZIKV
255 and mock TP and TN profiles at a CAM threshold of 80% show clearly that regions identified by the
256 thresholded ZIKV CAM have significantly increased ER density when comparing TP to TN frames
257 (Figure 8B, left). Conversely, regions identified by the thresholded mock CAM have increased ER
258 density for TN compared to TP cells (Figure 8B, right). We then calculated the average Euclidean
259 distance between the weighted center of mass of the CAMs and the weighted center of mass for
260 all ERmoxGFP labelled pixels (Figure 8C). The center of mass of the ZIKV CAM for TP and for the
261 mock CAM for TN were closest to the ERmoxGFP center of mass. As for the ER density profile of the
262 CAMs, Euclidean distance of FPs for the ZIKV CAM matched TP, and FNs for the mock CAM matched
263 TNs. Together, these data argue that the CAMs used to identify ZIKV- and mock-infected cells are
264 located in dense ER regions near the center of mass of the ERmoxGFP label.

265 To determine the relationship of the ZIKV CAM to the dense tubular matrix region that we iden-
266 tified by 3D STED super-resolution microscopy (Figure 3), we assessed CAM overlap with dsRNA,
267 NS2B, NS4B and ERmoxGFP labeling. To do this, we calculated the normalized CAM intensity, de-
268 fined as the intensity sum of a given channel in the ZIKV CAM normalized by the total area of that
269 channel. The 80% ZIKV CAM shows a higher degree of overlap with the NS4B- positive ER relative
270 to the ERmoxGFP-, dsRNA- and NS2B-labeled ER (Figure 9A, left). Further, based on Euclidean dis-
271 tance analysis, the center of mass of the ZIKV CAM was closer to the NS4B center of mass (Figure
272 9A, right). Relative to NS2B and dsRNA, NS4B density is present throughout the CER and increased
273 in the PER (Figure 5). Therefore, to further define the ER zone contributing to CNN discrimination
274 of ZIKV-infected cells, we assessed overlap of the ZIKV CAM with the dsRNA-positive and dsRNA-
275 negative CER as well as the PER, as defined previously (Figure 3). The PER, determined based on
276 Z-height of ER segments, includes the subnuclear ER and to ensure we were assessing strictly the
277 PER we segmented out the nuclear region using a semi-automated annotation approach (See Ma-
278 terials and Methods). As seen in Figure 9B, the ZIKV CAM shows increased overlap and proximity
279 with the dsRNA-positive CER relative to either the dsRNA-negative CER or PER. The region closest
280 to and most overlapping with the ZIKV CAM is the nuclear region, cropped from the PER channel.
281 As the center of mass of the ZIKV CAM presents the shortest Euclidean distances to the dsRNA-
282 positive CER and the nucleus, this locates the ZIKV CAM center of mass to the perinuclear CER
283 region between the dense dsRNA-positive tubular matrix and the nucleus.

284 This can be visualized in Figure 9C, where increased grey scale density highlights the weighted
285 overlap of the ZIKV CAM with these four ER regions. Increased ZIKV CAM overlap with the dsRNA-
286 positive ER, the perinuclear zone of the dsRNA-negative CER as well as the nuclear zone adjacent
287 to this region can be clearly observed. The ZIKV CAM encompasses the dsRNA, NS2B and NS4B-
288 positive dense tubular matrix region that houses ZIKV replication factories, but also includes the
289 adjacent perinuclear region enriched for NS4B but not NS2B. Individual patches do not encompass
290 the totality of the CER (see Figure 7C) and the precise nature of the features that the CNN uses to
291 discriminate between ZIKV- and mock-infected cells remains to be determined. CAM localization
292 analysis shows that the neural network uses the same CER region that we have observed to be
293 modified upon ZIKV infection. Deep learning therefore has the ability to identify the ER morpho-
294 logical changes associated with ZIKV infection.

Discussion

296 ZIKV infection is characterized by re-organization of the ER to create replication factories and con-
297 voluted ER membranes involved in viral replication, whose ultrastructure has been elegantly char-
298 acterized by EM (19, 25). Here, 3D STED super resolution microscopy reveals the formation of a
299 novel, perinuclear, crescent-shaped region of dense tubular ER, or convoluted membranes, within
300 the CER of ZIKV-infected cells. This region is enriched for dsRNA and ZIKV non-structural proteins

301 NS2B and NS4B and therefore corresponds to the site of ZIKV replication factories and genomic
302 replication (19, 20). 3D STED microscopy therefore shows that ZIKV infection induces CER reorga-
303 nization. Importantly, based in large part on the formation of this dense CER region, deep learning
304 image analysis is able to identify ZIKV-infected cells based solely on ER morphology. This high-
305 lights the potential utility of ER reorganization as a sensitive host cell reporter for use in screens
306 for inhibitors of infection by ZIKV and other flaviviruses, as well as coronaviruses, such as severe
307 acute respiratory syndrome coronavirus 2 (SARS-CoV-2), that induce extensive ER rearrangement
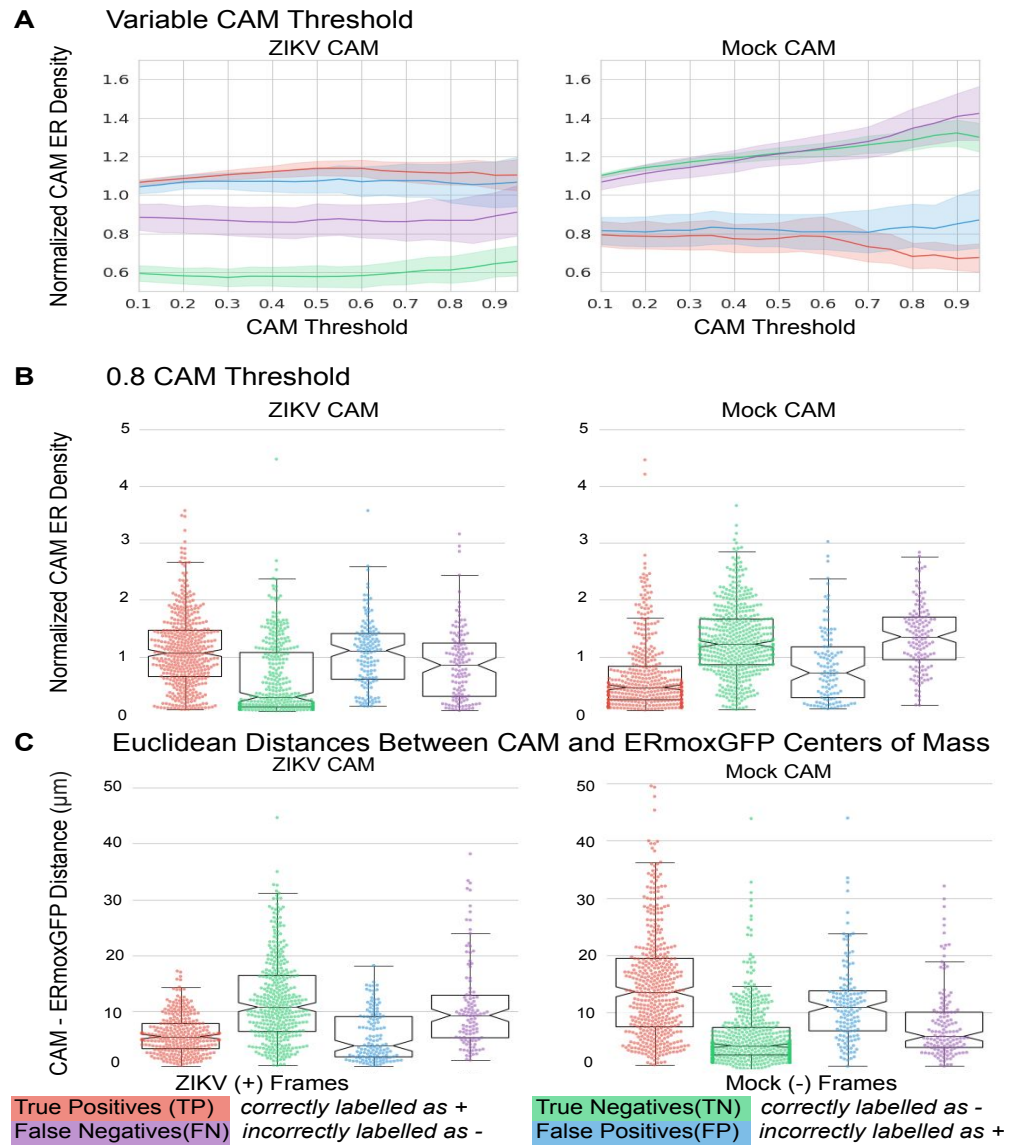
Figure 8. Normalized CAM ER density across subgroups. ROIs are defined by various CAM thresholds. For a given ROI, ER density is defined as total ERmoxGFP intensity within the ROI divided by ERMoxGFP area inside the ROI. ER density for each ROI defined by the CAM is then normalized by the ER density of the whole cell. A) ER density of ROIs defined by CAM thresholds from 10-95% with increments of 5% is compared across 4 subgroups: ZIKV-infected 2D frames correctly predicted to be infected (true positives); mock-infected 2D frames correctly predicted to be uninfected (true negatives); ZIKV-infected 2D frames incorrectly predicted to be uninfected (false negatives); mock-infected 2D frames incorrectly predicted to be infected (false positives). B) ER densities of 80% CAMs ROIs compared across subgroups. C) Euclidean distances between center of mass of 80% CAMs ROIs and weighted center of mass of ERmoxGFP signal.

308 (15, 42).

309 The ER is a morphologically complex organelle, containing smooth ER tubules and ribosome-
310 studded rough ER sheets identified ultrastructurally by EM since over 60 years (43). In confocal im-
311 ages of cultured cells, these morphological structures correspond, respectively, to PER tubules and
312 the dense perinuclear CER (3). Here, we approximate CER and PER regions based upon Z bound-
313 ing box height of segmented 3D STED ER volumes and show that the dense ER zone enriched for
314 dsRNA is within the CER. The CER of both ZIKV- and mock-infected U87 cells is composed of tubular
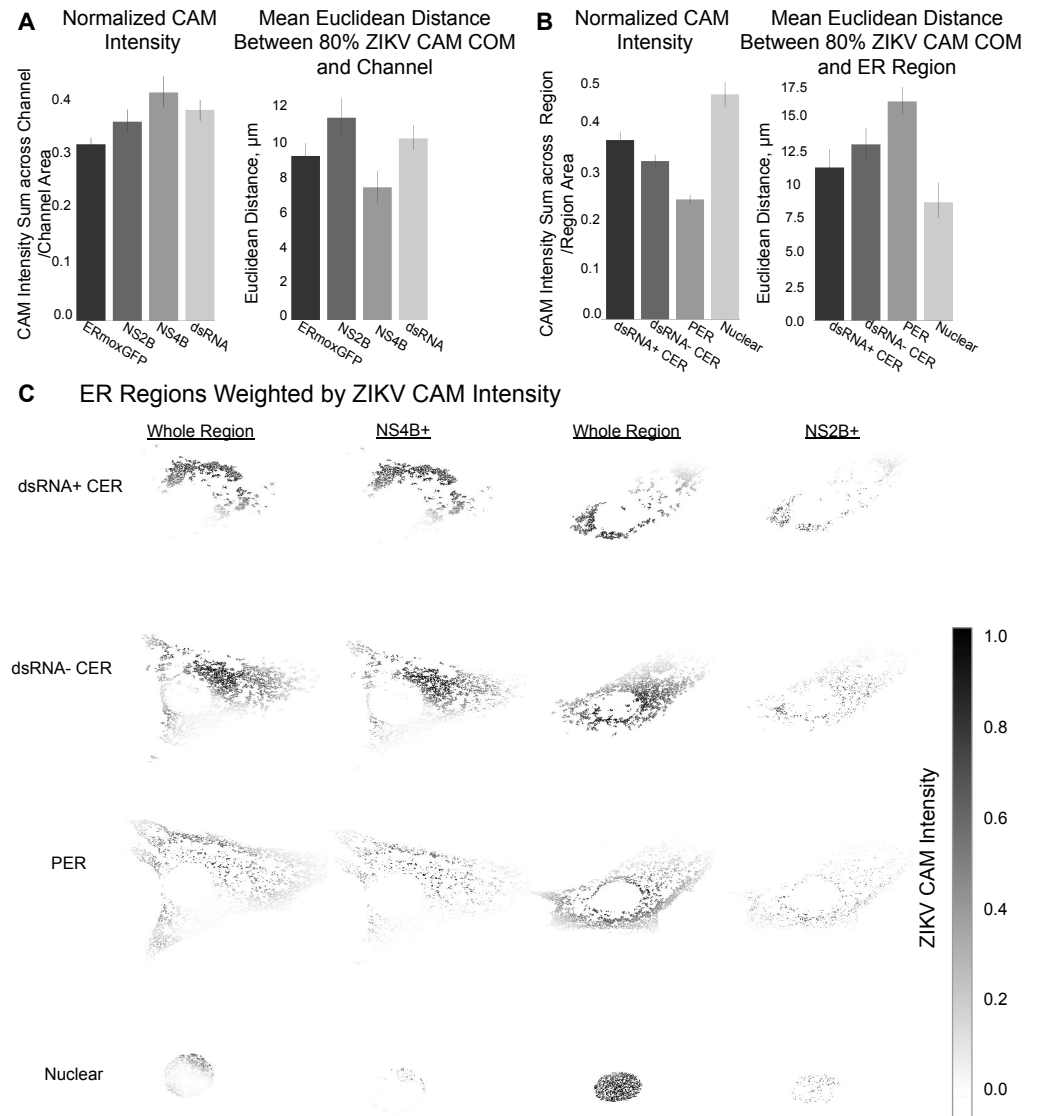
Figure 9. ZIKV CAM intensity relative to ER Regions. A) ZIKV CAM localization with respect to ERmoxGFP, dsRNA, NS4B and NS2B labelling. Left: Normalized CAM intensity refers to the total ZIKV CAM intensity colocalized with a given channel, normalized by the channel area. Mean Euclidean distances measured between the 80% ZIKV CAM region center of mass and all pixels of the indicated labelled protein. B) ZIKV CAM localization with respect to ER regions: dsRNA-positive CER (dsRNA+ CER), dsRNA-negative CER (dsRNA- CER), PER with nuclear region removed (PER), segmented nuclear PER region (nucleus). Same metrics are used as (B), replacing channels with ER regions. C) Representative images of NS2B and NS4B labelled ZIKV-infected cells with ER regions weighted by ZIKV CAM intensity. Darker pixels (closer to 1.0) reflect presence of ERmoxGFP and high ZIKV CAM intensity.

315 networks that correspond to previously described PER tubular matrices (7). While we were unable
316 to detect ER sheets by super-resolution analysis of cultured U87 cells, EM of brain organoids shows
317 the transformation of ER sheets to convoluted membranes upon ZIKV infection. This suggests that
318 organoid structures present more highly developed ER structures than cultured cells; application
319 of 3D live cell super-resolution analysis (44) to this model of the developing fetal brain, composed
320 of a heterogenous population of cell types, may lead to better definition of complex ER structures
321 and their dynamic transitions in response to stress, such as viral infection. Nevertheless, the fixed
322 cell 3D STED analysis applied here demonstrates that convoluted membranes associated with ZIKV
323 replication derive from tubular matrix reorganization in the CER.

324   The ZIKV-induced CER-localized, high ER density tubular matrices are enriched for dsRNA. As
325 dsRNA is specifically associated with viral replication, this localizes active replication factories to
326 this CER domain that therefore corresponds to convoluted membranes (19). Functionally, the for-
327 mation of tubular matrix is suggested to stabilize high curvature regions of the ER with increased
328 membrane surface area that act as a reservoir for membrane proteins and lipids (7). ZIKV-induced
329 dense tubular matrix may serve to provide material required for formation of replication facto-
330 ries and viral replication. Previously, tubular matrices were shown to shaped by both RTN and
331 ATL proteins (Nixon-Abell et al., 2016). Consistently, depletion of RTN3.1A, ATL2 and ATL3 have
332 been shown to reduce ER reorganization and replication of multiple flaviviruses, including ZIKV
333 (25, 45, 46). Here, NS2B and NS4B are shown to associate with the ZIKV-induced tubular matrix
334 and colocalize with dsRNA, localizing these proteins to replication factories. NS2B distribution is
335 highly restricted to the ZIKV-induced tubular matrix, consistent with NS2B recruitment of NS3 to
336 the ER and its role as a cofactor for NS3 protease function, necessary for ZIKV genomic replication
337 and polyprotein cleavage (25, 28, 47). In contrast, NS4B has been shown to be a multifunctional,
338 membrane protein involved in many processes of ZIKV infection and pathogenesis, including pro-
339 moting ER membrane proliferation, curvature of ER membranes to produce replication factories
340 and disruption of ER-mitochondria contacts allowing the virus to successfully subvert the host in-
341 nate immune response (26, 48, 49). Demonstration here that NS4B presents a broad distribution
342 throughout the ER is consistent with such a role and implicates NS4B in the ER reorganization that
343 leads to tubular matrix formation. A complete understanding of the spatial and temporal role of
344 NS and ER shaping proteins in ZIKV-induced tubular matrix formation remains to be determined.

345   We show that deep convolutional neural networks can accurately classify ZIKV- and mock-infected
346 cells based on ER labeling. Through the use of CAMs, we focus on regions which are more likely to
347 be used by the network to infer a class label. Importantly, our analysis shows that the VGG16 neu-
348 ral network uses dense ERmoxGFP in the CER as an indicator of ZIKV infection. This demonstrates
349 that the neural network is detecting the ZIKV-induced reorganization of the CER that leads to the
350 formation of the tubular matrix associated with ZIKV replication. Accuracy obtained for VGG16
351 classification of ZIKV-infected cells from 3D STED image stacks is comparable to prior classification
352 using VGG16. VGG16 achieved 79.2% accuracy when classifying disease (e.g., melanoma) versus
353 benign skin lesions from the ISIC 2016 challenge dataset of dermoscopy images (37, 50). Analysis of
354 dystrophic MRI data classified Duchenne and congenital muscular dystrophies with an accuracy of
355 84.1% using VGG16, which was boosted by 7.6% when implementing their improved CAM method
356 into a ResNet50 base model (51). For an entirely different task and dataset, VGG16 achieved highest
357 accuracy (92.6%) compared to ResNet50 (79.4%), when trained to classify histopathological breast
358 cancer images (as benign or malignant breast tissue) from the publicly available BreakHis Dataset
359 (38, 52). Here, our analysis of a novel 3D STED data set introduces a baseline for classification per-
360 formance for 3D super-resolution microscopy data sets that will be of service to other researchers
361 applying deep learning approaches to super-resolution microscopy.

362   The interpretability of artificial intelligence is an evolving field and we believe that interpretable
363 methods, such as Grad-CAM (53), are important tools for the understanding of deep neural net-
364 works applied to exploratory data sets. This approach has now allowed us to identify features of
365 discriminatory regions, and has not, to our knowledge, been applied to subcellular morphology,

366 nor to 3D super resolution images of the ER. Comparison of downsampled low-resolution images
367 from 2D sections of cells presenting ER reorganization into a denser CER tubular matrix was suf-
368 ficient to train the neural network to identify ZIKV-infected cells. This highlights the sensitivity of
369 deep learning image analysis and augurs well for future identification not only of tubular matrix
370 but also of the peripheral tubules, 3-way junctions, sheets and organelle contacts that comprise
371 the ER (54). However, defining the morphological characteristics associated with deep learning-
372 based decision making from isolated 2D patches of ER remains a challenge. Future application of
373 similar deep learning approaches to super-resolution 3D analysis of both fixed and live cells may
374 lead to novel understanding of the dynamic, local changes to ER morphology associated with the di-
375 verse functions of this cellular organelle. To the best of our knowledge, interpreting the network's
376 decisions is a novel approach to study ER morphology using deep learning.

377 Screening of siRNA or small molecule libraries to identify inhibitors of viral infection is a valid
378 and urgent research endeavour, given the current SARS-CoV-2 pandemic. Such high-throughput
379 screens require robust, sensitive assays to identify potential inhibitors for subsequent secondary
380 screens and drug development. The intent of this study is not the use of deep learning to identify
381 virus-infected cells (55) but rather the use of deep learning to identify and localize the morpholog-
382 ical features of the ER. This includes but is not limited to the central ER tubular matrices induced
383 by ZIKV infection and therefore, in combination with 3D super-resolution microscopy, has tremen-
384 dous potential to identify distinct, local morphological features of the ER and other cellular or-
385 ganelles. Nevertheless, application of a deep learning framework to host-cell ER labeling correctly
386 identified ZIKV-infected cells from 2D sections of downsampled STED super-resolution images; this
387 indicates that VGG16 and other deep CNN architectures are capable of finding discriminatory fea-
388 tures in lower resolution images for correct identification of infected cells. Importantly, our deep
389 learning approach is translatable to ER reorganization induced by other pathogenic human en-
390 veloped viruses. As for flaviviruses (i.e. ZIKV), the ER is the key replication site for coronaviruses,
391 likely including SARS-CoV-2 responsible for COVID-19, whose infection is also associated with ER
392 reorganization to form convoluted membranes (15, 42, 56). Deep learning analysis of host cell
393 reorganization of the ER may therefore represent a sensitive detection approach to identify virus-
394 infected cells.

Methods and Materials

Antibodies, plasmids, chemicals and viruses

397 ERmoxGFP was a gift from Dr. Erik Snapp (Albert Einstein College of ERmoxGFP was a gift from
398 Dr. Erik Snapp (Albert Einstein College of Medicine, presently at Howard Hughes Medical Institute,
399 Janelia Research Campus, Virginia) (Addgene plasmid #68072), and Sec61β-GFP from Dr. Gia Voeltz
400 (University of Colorado, Boulder). Mouse anti-dsRNA antibody (Cat#: J2-1904) was purchased from
401 Scicons English and Scientific Consulting, goat anti-rabbit Alexa Fluor 532 from ThermoFisher Sci-
402 entific (Cat#: A-11009), goat anti-mouse Alexa Fluor 568 from ThermoFisher Scientific (Cat#: A-
403 11031), and goat serum from Thermo Fisher Scientific (Cat#: 16210-064). Rabbit anti-NS2B (Cat#:
404 GTX133308) and NS4B (Cat#: GTX133321) were kindly provided by Genetex (Cat#: GTX133321).
405 16% paraformaldehyde (Cat#: 15710) and 25% glutaraldehyde (Cat#: 16220) were from Electron
406 Microscopy Sciences, USA. All other chemicals were obtained from Sigma. ZIKV strain (PRVABC59)
407 was obtained from ATCC (Cat#: VR-1843).

Cells and organoids

409 U87 MG cells from ATCC (Cat#: HTB-14) were grown at 37°C with 5% CO_2 in Gibco Minimum Es-
410 sential Media (MEM) (Cat#: 11095080) containing 10% FBS, 1% MEM non-essential amino acids
411 (Cat#: 11140050), and 1% sodium pyruvate (Cat#: 11360070) (ThermoFisher Scientific) unless oth-
412 erwise stated. Plasmids were transfected in U87 cells with Effectene (Qiagen, Germany) according
413 to the manufacturer's protocols. Following 24 hours of plasmid transfection cells were incubated

414 in MEM with 800 mg/mL of Geneticin (Cat#: 10131027) to select for transfected cells. Media was

415 changed every 24 hours for a week and then every 2 days. Once colonies grew to confluency the

416 resultant GFP positive cells were sorted by FACS. Plasmid stable lines were maintained in MEM with

417 400 mg/mL of Geneticin where media was changed every two days. Human pluripotent stem cell

418 (hPSC)-derived cerebral organoids were grown at 37°C with 5% CO2 in STEMdiff Cerebral Organoid

419 Kit cell culture media from STEMCELL Technologies Inc. (Cat#: 08570).

Immunofluorescence labeling

421 Cells grown on #1.5H coverslips (Paul Marienfeld GmbH & Co, Germany) for 24 hours were washed

422 once with phosphate buffered saline (PBS) and incubated with ZIKV, diluted in MEM, at a MOI of

423 1 for 48 hours. Then cells were: 1) fixed with 3% paraformaldehyde with 0.2% glutaraldehyde at

424 room temperature for 15 minutes and washed with PBS-CM (PBS supplemented with 1 mM CaCl2

425 and 10 mM MgCl2) (all PBS-CM washes consist of two quick washes and then two 5 minute washes

426 unless otherwise specified); 2) permeabilized with 0.2% Triton X-100 for 5 minutes followed by PBS-

427 CM washes; 3) quenched of glutaraldehyde aldehydes with 1 mg/mL of NaBH4 for 10 minutes and

428 washed with PBS-CM; 4) blocked with 10% Goat serum (ThermoFisher Scientific) and 1% bovine

429 serum albumin (Sigma) in PBS-CM for 1 hour; 5) incubated with primary antibodies in the same

430 blocking solution as described above for 1 hour at room temperature (RT) then washed quickly

431 with PBC-CM once followed by three 5 minute washes with Antibody Wash Buffer (20x SSC, 0.05%

432 Triton-X100 in Milli-Q H2O); 6) incubated with secondary antibodies in Antibody Buffer (1% BSA,

433 2% goat serum, 0.05% Triton-X100, 20X sodium/sodium citrate buffer in Milli-Q H2O) for 1 hour at

434 RT then washed quickly with PBS-CM once followed by six 10 minute washes with Antibody Wash

435 Buffer on a rocker; 7) rinsed with Milli-Q H2O and mounted with ProLong Diamond (ThermoFisher

436 Scientific) and cured for 24-48 hours at RT (6).

3D STED microscopy

438 3D STED imaging was performed with the 100X/1.4 Oil HC PL APO CS2 objective of a Leica TCS SP8

439 3X STED microscope (Leica, Germany) using white light laser excitation with HyD detectors, and

440 Leica Application Suite X (LAS X) software. Sample acquisition was done at a scan speed of 600Hz

441 with a line average of 6. Time-gated fluorescence detection was used to further improve lateral

442 resolution. GFP was excited at 488 nm and depleted using the 592 nm depletion laser. Alexa

443 Fluor 532 was excited at 528 nm, and Alexa Fluor 568 was excited at 577 nm. Both were depleted

444 using the 660 nm depletion laser. To avoid crosstalk, image stacks for each channel were acquired

445 sequentially, in the order of Alexa Fluor 568, Alexa Fluor 532 and then GFP. A step size of 210 nm

446 was utilized for 3D STED. Images were then deconvoluted using Huygens Professional software

447 (Scientific Volume Imaging). 3D STED ER segmentation and ER region mask generation were done

448 using Imaris x64 9.2.1. dsRNA associated ER and NS4B/NS2B associated ER regions were generated

449 by partial overlap analysis after surface generation. All data produced from Imaris were parsed and

450 analyzed with a custom made Jupyter notebook. Two-tailed unpaired Student's t-tests or ANOVA

451 with post-hoc Tukey HSD were done using Graph Pad Prism 6.0.

Transmission electron microscopy

453 63-day old cerebral organoids were infected with the PRVABC59 ZIKV strain, MOI of 1, for 48 hours.

454 Organoids were then processed by replacing media with the primary fixative [0.1 M sodium cacody-

455 late, 1.5% paraformaldehyde, 1.5% glutaraldehyde, pH 7.3, room temperature] (57) and allowed to

456 sit for 1 hour before placing them at 4°C overnight. The organoids were washed three times (10

457 minutes each wash) with buffer (0.1M sodium cacodylate) and then post-fixed for 1 hour on ice in

458 0.1M osmium tetroxide in 0.1M sodium cacodylate (pH7.3). They were then washed three times

459 with distilled water (10 min each wash, room temperature) and stained en bloc with 1% aqueous

460 uranyl acetate for 1 hour at room temperature. They were washed again three times with distilled

461 water and then dehydrated through an ascending concentration series of ethyl alcohol (30%, 50%,

462 70%, 95%, 100%), passed through two changes of propylene oxide, and then infiltrated overnight in
463 a 1:1 solution of propylene oxide:EMBED 812 resin. The organoids were then passed through two
464 changes of 100% EMBED resin, embedded and the resin polymerized at 60°C for 48 hours. Thin
465 sections were cut using a diamond knife and sections were collected on copper grids. The sections
466 were then stained with uranyl acetate and lead citrate, and images collected using a FEI tecnai G2
467 Spirit transmission electron microscope operated at 120 kV.

Image data processing for CNN analysis

469 A custom pipeline was created using MATLAB R2019a (The Mathworks, Inc., Natick, MA) and Python
470 3 (Python Software Foundation, Scotts Valley, CA) scripts to convert data stored in Leica proprietary
471 format (.lif) to an accessible and lightweight format, which could easily feed as input to state of the
472 art CNNs. Once an imaging session is complete, the biologist exports Leica STED data without
473 need for further processing or file conversion. The pipeline takes Leica .lif files of 3D STED vol-
474 umes of multiple cells as input and outputs a single NumPy array per cell. The pipeline relies on
475 open-source Matlab package Bio-Formats, modified to handle our needs. This pipeline has been
476 validated through manually inspection of cells with Imaris image rendering software.

Deep learning

478 The Keras open-source neural network library was used to modify and train neural networks us-
479 ing Tensorflow backend. VGG16 was used as a base model to predict infected from non-infected
480 2D frames (removing the original fully-connected output layers). This architecture and pretrained
481 weights (learned using the ImageNet dataset) are easily accessible using Keras. The pretrained
482 weights can be loaded when instantiating the base model. On top of the VGG16 max pooling layer,
483 we add (in order): a global average pooling layer, a dropout layer (with a dropout rate of 0.5), dense
484 layer (using ReLu activation, output dimension 1024), a second dropout layer (0.5 dropout rate) fol-
485 lowed by a final dense layer (with softmax activation) for making predictions. These additional
486 layers helped prevent overfitting of the CNN to the training data.

487 56 individual CNNs (with identical architecture as outlined above) were trained using a softmax
488 loss function and RMSprop optimizer. Each model was then used to predict the class labels (i,e.
489 assign either 'Mock' or 'ZIKV' to each 2D frame) of a single test cell. The CNNs were fine-tuned for
490 a total of 24 epochs, after which only the best weights (resulting in highest classification perfor-
491 mance on the validation set) were then reloaded during test time. CAMs were generated following
492 the procedure outlined by (39), where global average pooling is applied to the output of the final
493 convolutional layer of VGG16 followed by a weighted sum, according to the specified class (e.g.,
494 ZIKV). Models were trained on 2 Nvidia GPUs (GeForce GTX TITAN X, each with 32 GB of RAM).

495 ROIs generated through the deep learning framework were analyzed using python program-
496 ming. Statistical analysis across channels and ER regions relied on several open-source python
497 packages. SciPy's statistical functions module, was used to perform Kruskal-Wallis non-parametric
498 tests, statsmodules python module was used for One-way ANOVA, and scikit-posthocs python pack-
499 age was used to perform Dunn's post hoc test.

Code availability

501 All code related to data processing and deep learning and was written using open-source packages.
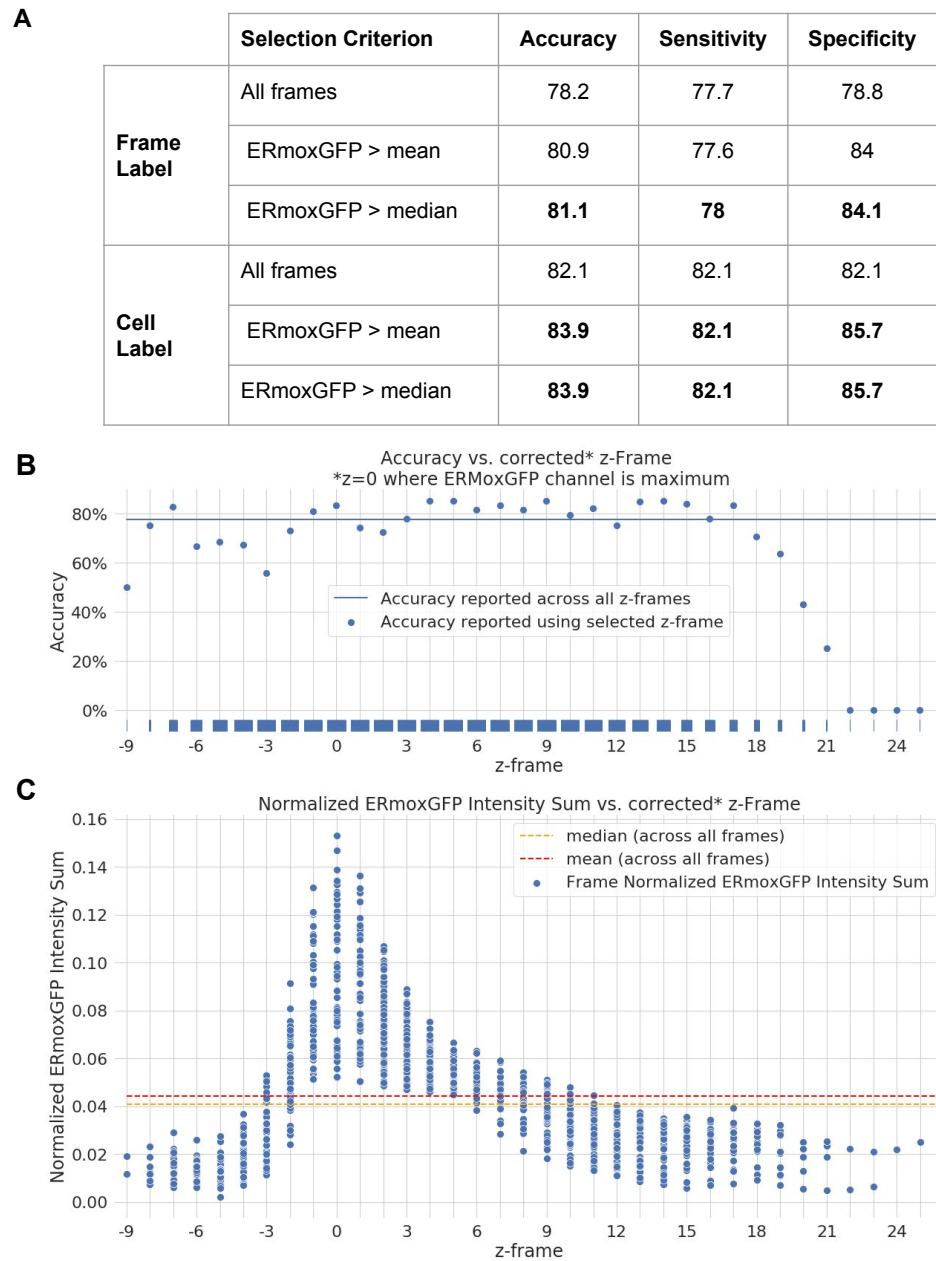
References

515 **References**

516 **1. Terasaki M**, Chen LB, Fujiwara K. Microtubules and the endoplasmic reticulum are highly inter-
517 dependent structures. Journal of Cell Biology. 1986;103:1557-68.

518 **2. Shibata Y**, Voeltz GK, Rapoport TA. Rough sheets and smooth tubules. Cell. 2006;126(3):435-9.

519 **3. Shibata Y**, Shemesh T, Prinz WA, Palazzo AF, Kozlov MM, Rapoport TA. Mechanisms determining
520 the morphology of the peripheral ER. Cell. 2010;143(5):774-88.

521 **4. Voeltz GK**, Prinz WA, Shibata Y, Rist JM, Rapoport TA. A class of membrane proteins shaping the
522 tubular endoplasmic reticulum. Cell. 2006;124(3):573-86.

523 **5. Schroeder LK**, Barentine AES, Merta H, Schweighofer S, Zhang Y, Baddeley D, et al. Dynamic
524 nanoscale morphology of the ER surveyed by STED microscopy. J Cell Biol. 2019;218(1):83-96.

525 **6. Gao G**, Zhu C, Liu E, Nabi IR. Reticulon and CLIMP-63 control nanodomain organization of pe-
526 ripheral ER tubules. PLOS Biology. 2019;17(8):e3000355.

527 **7. Nixon-Abell J**, Obara CJ, Weigel AV, Li D, Legant WR, Xu CS, et al. Increased spatiotemporal reso-
528 lution reveals highly dynamic dense tubular matrices in the peripheral ER. Science. 2016;354(6311):
529 3928.

530 **8. Paul D**, Bartenschlager R. Architecture and biogenesis of plus-strand RNA virus replication fac-
531 tories. World J Virol. 2013;2(2):32-48.

532 **9. Kato H**, Takahasi K, Fujita T. RIG-I-like receptors: cytoplasmic sensors for non-self RNA. Immunol
533 Rev. 2011;243(1):91-8.

534 **10. Binder M**, Eberle F, Seitz S, Mucke N, Huber CM, Kiani N, et al. Molecular mechanism of signal
535 perception and integration by the innate immune sensor retinoic acid-inducible gene-I (RIG-I). J Biol
536 Chem. 2011;286(31):27278-87.

537 **11. Tsai AY**, English BC, Tsolis RM. Hostile Takeover: Hijacking of Endoplasmic Reticulum Function
538 by T4SS and T3SS Effectors Creates a Niche for Intracellular Pathogens. Microbiol Spectr. 2019;7(3).

539 **12. Romero-Brey I**, Bartenschlager R. Endoplasmic Reticulum: The Favorite Intracellular Niche for
540 Viral Replication and Assembly. Viruses. 2016;8(6).

541 **13. Roy CR**, Salcedo SP, Gorvel JP. Pathogen-endoplasmic-reticulum interactions: in through the
542 out door. Nat Rev Immunol. 2006;6(2):136-47.

543 **14. Mackenzie JM**, Jones MK, Young PR. Immunolocalization of the dengue virus nonstructural
544 glycoprotein NS1 suggests a role in viral RNA replication. Virology. 1996;220(1):232-40.

545 **15. Fung TS**, Liu DX. Human Coronavirus: Host-Pathogen Interaction.
546 Annu Rev Microbiol. 2019;73:529-57.

547 **16. Carteaux G**, Maquart M, Bedet A, Contou D, Brugieres P, Fourati S, et al. Zika Virus Associated
548 with Meningoencephalitis. N Engl J Med. 2016;374(16):1595-6.

549 **17. Mlakar J**, Korva M, Tul N, Popovic M, Poljsak-Prijatelj M, Mraz J, et al. Zika Virus Associated with
550 Microcephaly. N Engl J Med. 2016;374(10):951-8.

551 **18. Fauci AS**, Morens DM. Zika Virus in the Americas–Yet Another Arbovirus Threat. N Engl J Med.
552 2016;374(7):601-4.

553 **19. Cortese M,** Goellner S, Acosta EG, Neufeldt CJ, Oleksiuk O, Lampe M, et al. Ultrastructural
554 Characterization of Zika Virus Replication Factories. Cell Rep. 2017;18(9):2113-23.

555 **20. Offerdahl DK,** Dorward DW, Hansen BT, Bloom ME. Cytoarchitecture of Zika virus infection in
556 human neuroblastoma and Aedes albopictus cell lines. Virology. 2017;501:54-62.

21. **Hanners NW,** Eitson JL, Usui N, Richardson RB, Wexler EM, Konopka G, et al. Western Zika Virus in Human Fetal Neural Progenitors Persists Long Term with Partial Cytopathic and Limited Immunogenic Effects. Cell Rep. 2016;15(11):2315-22.

22. **Bartenschlager R,** Miller S. Molecular aspects of Dengue virus replication. Future Microbiol. 2008;3(2):155-65.

23. **Nitatpattana N,** Chaiyo K, Rajakam S, Poolam K, Chansiprasert K, Pesirikan N, et al. Complete Genome Sequence of a Zika Virus Strain Isolated from the Serum of an Infected Patient in Thailand in 2006. Genome Announc. 2018;6(10).

24. **Neufeldt CJ,** Cortese M, Acosta EG, Bartenschlager R. Rewiring cellular networks by members of the Flaviviridae family. Nat Rev Microbiol. 2018;16(3):125-42.

25. **Aktepe TE,** Liebscher S, Prier JE, Simmons CP, Mackenzie JM. The Host Protein Reticulon 3.1A Is Utilized by Flaviviruses to Facilitate Membrane Remodelling. Cell Rep. 2017;21(6):1639-54.

26. **Chatel-Chaix L,** Cortese M, Romero-Brey I, Bender S, Neufeldt CJ, Fischl W, et al. Dengue Virus Perturbs Mitochondrial Morphodynamics to Dampen Innate Immune Responses. Cell Host Microbe. 2016;20(3):342-56.

27. **Welsch S,** Miller S, Romero-Brey I, Merz A, Bleck CK, Walther P, et al. Composition and three-dimensional architecture of the dengue virus replication and assembly sites. Cell Host Microbe. 2009;5(4):365-75.

28. **Xing H,** Xu S, Jia F, Yang Y, Xu C, Qin C, et al. Zika NS2B is a crucial factor recruiting NS3 to the ER and activating its protease activity. Virus Res. 2020;275:197793.

29. **Costantini LM,** Baloban M, Markwardt ML, Rizzo M, Guo F, Verkhusha VV, et al. A palette of fluorescent proteins optimized for diverse cellular environments. Nature Communications. 2015;6(1):7670.

30. **Lewis MJ**, Pelham HR. Ligand-induced redistribution of a human KDEL receptor from the Golgi complex to the endoplasmic reticulum. Cell. 1992;68(2):353-64.

31. **Loewen CJ,** Roy A, Levine TP. A conserved ER targeting motif in three families of lipid binding proteins and in Opi1p binds VAP. Embo J. 2003;22(9):2025-35.

32. **Qian X,** Nguyen HN, Jacob F, Song H, Ming GL. Using brain organoids to understand Zika virus-induced microcephaly. Development. 2017;144(6):952-7.

33. **Russakovsky O,** Deng J, Su H, Krause J, Satheesh S, Ma S, et al. ImageNet Large Scale Visual Recognition Challenge. arXiv. 2015;1409.0575.

34. **Krizhevsky A,** Sutskever I, Hinton GE. Imagenet classification with deep convolutional neural networks. Advances in neural information processing systems 2012:1097-105.

35. **Simonyan K,** Zisserman A. Very deep convolutional networks for large-scale image recognition. arXiv preprint arXiv. 2014;1409:1556.

36. **Tan M,** Le Q. EfficientNet: Rethinking Model Scaling for Convolutional Neural Networks. arXiv. 2019;1905.11946.

37. **Codella NC,** Gutman D, Celebi ME, Helba B, Marchetti MA, Dusza SW, et al., editors. Skin lesion analysis toward melanoma detection: A challenge at the 2017 international symposium on biomedical imaging (isbi), hosted by the international skin imaging collaboration (isic). 2018 IEEE 15th International Symposium on Biomedical Imaging (ISBI 2018); 2018: IEEE.

38. **Spanhol FA,** Oliveira LS, Petitjean C, Heutte L. A dataset for breast cancer histopathological image classification. IEEE Transactions on Biomedical Engineering. 2015;63(7):1455-62.

39. **Zhou B,** Khosla A, Lapedriza A, Oliva A, Torralba A. Learning Deep Features for Discriminative Localization. Computer Vision and Pattern Recognition. 2016.

40. **Ciocca G,** Mazzini D, Schettini R, editors. Evaluating CNN-based semantic food segmentation across illuminants. International Workshop on Computational Color Imaging; 2019: Springer.

41. **Nguyen H-G,** Pica A, Hrbacek J, Weber DC, La Rosa F, Schalenbourg A, et al., editors. A novel segmentation framework for uveal melanoma in magnetic resonance imaging based on class activation maps. International Conference on Medical Imaging with Deep Learning; 2019.

42. **Fung TS,** Liu DX. Coronavirus infection, ER stress, apoptosis and innate immunity. Front Microbiol. 2014;5:296.

43. **Palade GE,** Porter KR. Studies on the endoplasmic reticulum. I. Its identification in cells in situ. J Exp Med. 1954;100(6):641-56.

44. **Valm AM,** Cohen S, Legant WR, Melunis J, Hershberg U, Wait E, et al. Applying systems-level spectral imaging and analysis to reveal the organelle interactome. Nature. 2017;546(7656):162-7.

45. **Monel B,** Rajah MM, Hafirassou ML, Sid Ahmed S, Burlaud-Gaillard J, Zhu P-P, et al. Atlastin Endoplasmic Reticulum-Shaping Proteins Facilitate Zika Virus Replication. Journal of Virology. 2019;93(23):e010 19.

46. **Neufeldt CJ,** Cortese M, Scaturro P, Cerikan B, Wideman JG, Tabata K, et al. ER-shaping atlastin proteins act as central hubs to promote flavivirus replication and virion assembly. Nat Microbiol. 2019;4(12):2416-29.

47. **Zhang Z,** Li Y, Loh YR, Phoo WW, Hung AW, Kang C, et al. Crystal structure of unlinked NS2B-NS3 protease from Zika virus. Science. 2016;354(6319):1597-600.

48. **Zmurko J,** Neyts J, Dallmeier K. Flaviviral NS4b, chameleon and jack-in-the-box roles in viral replication and pathogenesis, and a molecular target for antiviral intervention. Rev Med Virol. 2015;25(4):205-23.

49. **Liang Q,** Luo Z, Zeng J, Chen W, Foo SS, Lee SA, et al. Zika Virus NS4A and NS4B Proteins Deregulate Akt-mTOR Signaling in Human Fetal Neural Stem Cells to Inhibit Neurogenesis and Induce Autophagy. Cell Stem Cell. 2016;19(5):663-71.

50. **Menegola A,** Fornaciali M, Pires R, Bittencourt FV, Avila S, Valle E, editors. Knowledge transfer for melanoma screening with deep learning. 2017 IEEE 14th International Symposium on Biomedical Imaging (ISBI 2017); 2017: IEEE.

51. **Cai J,** Xing F, Batra A, Liu F, Walter GA, Vandenborne K, et al. Texture analysis for muscular dystrophy classification in MRI with improved class activation mapping. Pattern recognition. 2019;86:368-75.

52. **Mehra R,** Breast cancer histology images classification: Training from scratch or transfer learning? ICT Express. 2018;4(4):247-54.

53. **Selvaraju R,** Cogswell M, Das A, Vedantam R, Parikh D, Batra D. Grad-CAM: Visual Explanations from Deep Networks via Gradient-based Localization. arViv. 2016;1610.02391.

54. **Westrate LM,** Lee JE, Prinz WA, Voeltz GK. Form follows function: the importance of endoplasmic reticulum shape. Annu Rev Biochem. 2015;84:791-811.

55. **Fisch D,** Yakimovich A, Clough B, Wright J, Bunyan M, Howell M, et al. Defining host–pathogen interactions employing an artificial intelligence workflow. eLife. 2019;8:e40560.

56. **Knoops K,** Kikkert M, Worm SH, Zevenhoven-Dobbe JC, van der Meer Y, Koster AJ, et al. SARS-coronavirus replication is supported by a reticulovesicular network of modified endoplasmic reticulum. PLoS Biol. 2008;6(9):e226.

57. **Lyon K,** Adams A, Piva M, Asghari P, Moore ED, Vogl AW. Ca2+ signaling machinery is present at intercellular junctions and structures associated with junction turnover in rat Sertoli cells. Biol Reprod. 2017;96(6):1288-302.

Supplemental Figure I: Network Performance Analysis

A

	Selection Criterion	Accuracy	Sensitivity	Specificity
Frame Label	All frames	78.2	77.7	78.8
	ERmoxGFP > mean	80.9	77.6	84
	ERmoxGFP > median	**81.1**	**78**	**84.1**
Cell Label	All frames	82.1	82.1	82.1
	ERmoxGFP > mean	**83.9**	**82.1**	**85.7**
	ERmoxGFP > median	**83.9**	**82.1**	**85.7**

B

C

Figure 10. Network Performance Analysis A) Performance metrics are reported across predictions of frame labels and cell labels, where cell labels correspond to the majority label of predicted frame labels for each cell. Results are reported using a given selection criteria: using all frames (rows 1, 4), using only frames with normalized ERmoxGFP signal greater than mean normalized ERmoxGFP signal (rows 2, 5) or greater than median normalized ERmoxGFP signal (rows 3, 6). Mean and median thresholds are computed on a cell basis. The rug plot (above x-axis) visualises distribution of z-frames. B) Accuracy reported across corrected z-frames, z=0 is where normalized ERmoxGFP Intensity Sum is maximal. C) Normalized ERmoxGFP Intensity sum plotted against corrected z-frame. Dashed lines indicate the median (orange) and mean (red) Normalized ERmoxGFP Intensity sum computed across all frames.